Review of Scientific Instruments

Tunable homogeneous kG magnetic field production using permanent magnets

Cite as: Rev. Sci. Instrum. **92**, 123002 (2021); https://doi.org/10.1063/5.0064498
Submitted: 23 July 2021 • Accepted: 21 November 2021 • Published Online: 06 December 2021

Danielle Pizzey

Review of Scientific Instruments ARTICLE scitation.org/journal/rsi

Tunable homogeneous kG magnetic field production using permanent magnets

Cite as: Rev. Sci. Instrum. 92, 123002 (2021); doi: 10.1063/5.0064498
Submitted: 23 July 2021 • Accepted: 21 November 2021 •
Published Online: 6 December 2021

Danielle Pizzey[a)]

AFFILIATIONS

Department of Physics, Joint Quantum Centre (JQC) Durham-Newcastle, Durham University, South Road, Durham DH1 3LE, United Kingdom

[a)]Author to whom correspondence should be addressed: danielle.boddy@durham.ac.uk

ABSTRACT

We present a permanent ring magnet arrangement that can achieve a tunable axial magnetic field from 1.80(5) to 2.67(9) kG. The apparatus has been designed to accommodate a cylindrical atomic vapor cell of length 25 mm and diameter 25 mm to lie within the bore of the ring magnets, providing an alternative route for imaging through atomic vapors in large magnetic fields. The measured axial magnetic field has an rms variation of less than 4% over the length of vapor cell, while the calculated field inhomogeneity is less than 5% radially and 12% longitudinally across a cylindrical volume with diameter 20 mm and length 25 mm. The instrument consists of layered concentric off-the-shelf N42 neodymium–iron–boron axially magnetized ring magnets. The magnets are organized into four cylindrical brass holders, whose relative separation can be manipulated to achieve the desired magnetic field strength. We present magnetic field computations and Marquardt–Levenberg fits to experimental data and demonstrate excellent agreement between theory and experiment.

I. INTRODUCTION

There are a vast number of situations in experimental atomic and optical physics where magnetic fields are utilized, from a Zeeman slower necessary to slow and cool an atomic beam[1,2] to magneto-optical filters (MOFs) that use thermal atomic vapors in magnetic fields.[3] MOFs find a wide range of applications in other disciplines, including quantum key distribution,[4] optical isolators,[5] atmospheric LIDAR,[6,7] and laser frequency stabilization.[8,9] In certain cases, there is the need to produce large uniform magnetic fields (i.e., >1 kG) in order to study a specific branch of physics, in particular, thermal vapor experiments working in the hyperfine Paschen–Back regime.[10,11] It is not an easy feat to produce large uniform magnetic fields: a work-around is typically to reduce the physical dimensions of the interrogation region over which the experiments are performed.[12,13] However, this is not applicable to all situations, and the need to produce large magnetic fields over increasingly large length-scales is ever pressing. A particular example is the use of solar filters in solar flare forecasting.[14–17] A solar filter consists of two cascaded atomic vapor cells, each within a longitudinal magnetic field,[18,19] that are mounted on a telescope for solar monitoring. The best working parameters (i.e., the longitudinal magnetic field, vapor cell length, and vapor temperature) of the solar filter depend on the atomic species; these parameters can be determined theoretically using a modified version of ElecSus[20] (a software package that calculates the electric susceptibility of an atomic medium). Often, solar filters require longitudinal magnetic fields of several kilogauss that are uniform over the length of the atomic vapor cell, which is typically tens of millimeters.[21] Furthermore, owing to optical design constraints, the size of the interrogating beam through the solar filter typically has an area of several millimeters. For this reason, the magnetic field needs to be homogeneous in the radial direction also.

Magnetic fields can be produced via an electromagnet, which uses a coil of wire and a current supply, or by using a permanent magnet. There are many pros and cons to choosing either method. One particular benefit of using the electromagnet is the ability to tune the magnetic field by simply changing the current supplied to the coil; this is advantageous when testing a new idea or characterizing an experiment. To produce magnetic fields of several kilogauss using electromagnets, the coils will typically heat up during continuous operation.[22–24] This can be favorable if the atomic vapor cell requires heating also; however, in some scenarios, having independent control of the magnetic field strength and atomic vapor

cell temperature is necessary. On the flip side, permanent magnet arrangements neither have any power requirements, hence no cooling, nor do they suffer from magnetic field noise due to current fluctuations originating from the power supplies. There are some disadvantages, however. To produce kG fields, it is necessary to use magnets with a high remanence magnetic field. Of all the commercially available magnets, neodymium–iron–boron (NdFeB) magnets have the highest remanence field but at the expense of having a comparatively lower Curie temperature (≈300 °C)[25] and being more brittle with respect to other magnetic materials. When designing a permanent magnet instrument, it is vital to have an appreciation of the environment the magnets will be working in, as this will be a deciding factor on the chosen magnetic material and strength. For the application of solar filters, a "set and forget" approach is ideal when making a system transportable and controlled remotely, as this reduces the number of potential technical failures during fieldwork. It is for this reason that we have opted to pursue the permanent magnet route. With appropriately designed hardware, we address the tunability problem and demonstrate field homogeneity over the required length-scale.

The remainder of this paper is organized as follows: in Sec. II A, we present the magnetic field computation; Sec. II B discusses the functionality of the hardware and limitations to the maximum achievable magnetic field; we illustrate the performance of the assembly in Sec. III; and finally, conclusions are drawn and an outlook is provided in Sec. IV.

II. DESIGN OVERVIEW

The instrument is designed such that there is a maximum axial magnetic field of ≈2.7 kG, a field heterogeneity (defined in Sec. II A) of less than 10% over a cylindrical volume of length 25 mm and diameter 20 mm, and an ≈1 kG tuning range of the longitudinal magnetic field strength.

A. Magnetic field computation

Finding a permanent magnet arrangement that abides by the constraints stated in Sec. II is a complex task. There are many software packages available that enable the magnetic field to be determined: we chose to use MagPyLib,[26] which is a python package for magnetic field computation. The MagPyLib package is open source and provides visual aids of the magnet geometry, which assisted the design of the hardware mount.

The criteria of the instrument state that there must be a cylindrical volume over which the field heterogeneity is minimal and space available to accommodate a cylindrical atomic vapor cell. Since the magnetic field is a vector quantity, $\mathbf{B} \equiv (B_x, B_y, B_z)$, using magnets with cylindrical symmetry will make the design simpler as we only need to consider the longitudinal and radial components of the magnetic field. We focus our studies on ring magnets with opposite polarity on opposite faces as this produces an axial magnetic field.

In order to design an appropriate magnet assembly, we must first understand the magnetic field profile of a single ring magnet. Figure 1 illustrates the magnetic field profile of a ring magnet with outer diameter (OD) $2R_o$, inner diameter (ID) $2R_i$, length $2d$, and a remanence field B_0 = 12.8 kG, which is typical of N42 grade neodymium–iron–boron (NdFeB) magnets.[27] The magnet dimensions, as shown in Fig. 1(a), and the remanence field have been chosen to mimic those used in the instrument so that direct comparisons can be made. In Fig. 1(b)(i), the magnetic field profile, which has been calculated using the MagPyLib package, is shown in the x–z plane, and due to cylindrical symmetry, the profile is identical in the y–z plane also. The arrows demonstrate the field direction, while the color of the arrow represents the magnitude of the field. Inside the physical profile of the magnet, the field is strongest. Within the bore of the ring magnet, we see that the field is the opposite to that inside the magnet and a lot weaker, as evidenced by the change in color of the arrow.

We have chosen a design that uses axially magnetized magnets since we are interested in a longitudinal magnetic field. Irrespective of this, there will still be a radial component of the magnetic field present. It is important to know how the radial component compares to the longitudinal field and whether it is of significance to the total magnitude of the field.

Figure 1(b)(ii) illustrates the radial component, B_x, (top panel) and the longitudinal component, B_z, (middle panel) as a function of radial distance from the axis for the magnet geometry shown in Fig. 1(a). On axis, the radial component of the field is always zero, regardless of the longitudinal position within the magnet. This is also true in the very center of the magnet, i.e., at $z = 0$, and is valid for all radial positions, not just on axis. Off axis and when $z \neq 0$, the radial component is non-zero and increases as we move further from the axis. Since the magnitude of the total magnetic field at a particular point in space, $\mathbf{B}_{\text{total}}(x, y, z)$, is given by

$$|\mathbf{B}_{\text{total}}(x,y,z)| = \sqrt{[B_x(x,y,z)]^2 + [B_y(x,y,z)]^2 + [B_z(x,y,z)]^2}, \tag{1}$$

we see that the radial component contributes to, at most, 10% (i.e., at $x = R_i$) of the field magnitude, as shown in the lower panel of Fig. 1(b)(ii).

To determine the uniformity of the magnetic field over the cylindrical volume of interest, we must calculate the field heterogeneity. The heterogeneity $h(x, y, z)$ can be quantified as

$$h(x,y,z) \equiv \frac{|\mathbf{B}(x,y,z) - \mathbf{B}(0,0,0)|}{|\mathbf{B}(0,0,0)|}, \tag{2}$$

where $\mathbf{B}(x, y, z)$ is the field vector at a particular point in space and $\mathbf{B}(0, 0, 0)$ is the reference magnetic field at the center of symmetry.[28,29] Figures 1(c)(i) and 1(c)(ii) illustrate the longitudinal and radial field heterogeneity for the magnet shown in Fig. 1(a). We see in Fig. 1(c)(i) that there is a 10% field variation within the spatial constraints $\frac{+R_i}{2} \geq x, z \geq \frac{-R_i}{2}$. Similarly, in Fig. 1(c)(ii), there is a 10% field variation within the spatial constraints $\frac{+R_i}{2} \geq x, y \geq \frac{-R_i}{2}$ also.

This simple picture aids our understanding of the magnetic field profile of ring magnets. There are two take home messages that we learn from Fig. 1. First, there will always be a reduction in the field strength and a flip of the field direction on the axis of the ring magnet upon exit of the bore of the magnet, as evidenced in Fig. 1(b). To produce a longitudinal field heterogeneity of ≤10%, the length of the ring magnet should be twice that of the spatial extent of field homogeneity. In our case, we require the total length ($2d$) of the magnet assembly to be 50 mm since our region-of-interest cylinder is 25 mm in length. Second, there will always be a radial component of the field. To produce a radial field heterogeneity of ≤10%, the inner diameter of the magnets should be twice that of the spatial

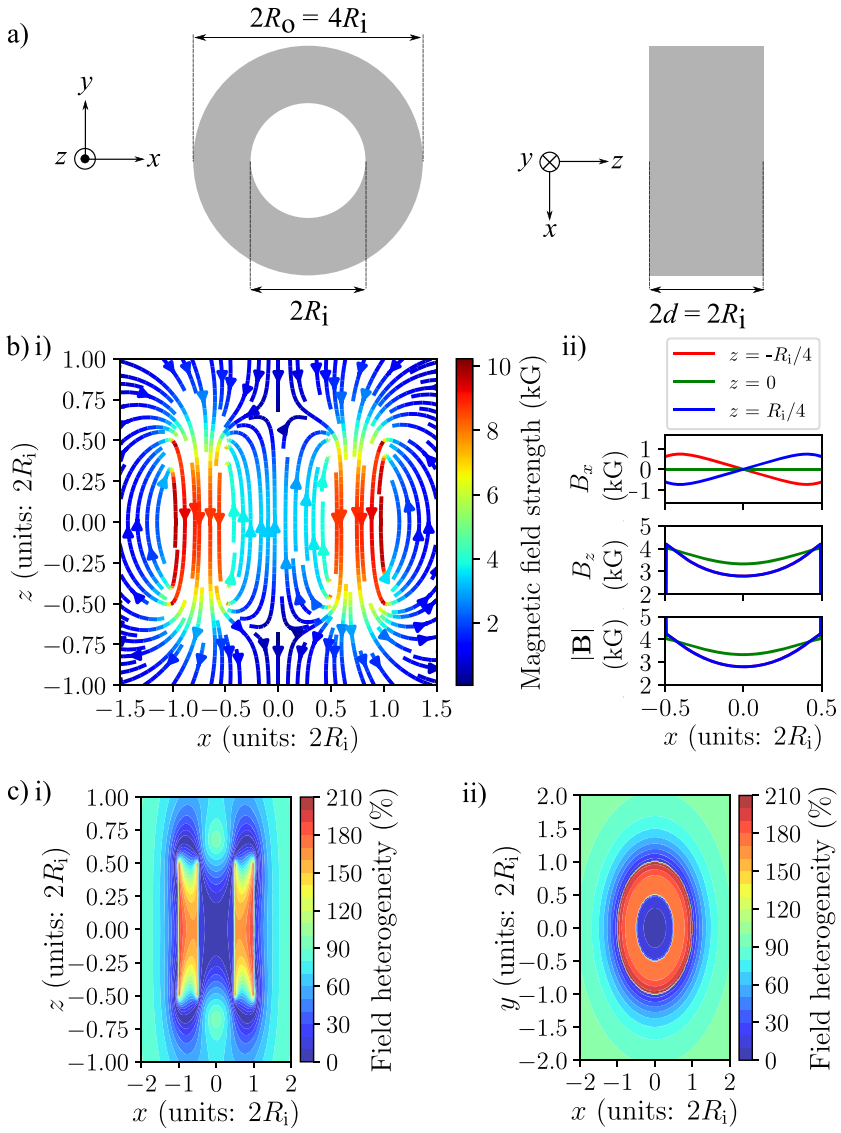

FIG. 1. Simple schematic of (a) a ring magnet with outer diameter $2R_o$, inner diameter $2R_i$, thickness $2d$, and remanence field B_0 = 12.8 kG, typical of N42 grade NdFeB magnets[27] and the associated (b) magnetic field profile calculated using MagPyLib.[26] (i) The arrows represent the direction of the magnetic field vector, while the color and corresponding colorbar indicate the magnitude of the magnetic field. (ii) Slices of (i) taken at $z = -R_i/4$, 0, and $+R_i/4$, represented by red, green, and blue lines, respectively. The radial component, B_x, longitudinal component, B_z, and magnetic field magnitude, $|\mathbf{B}|$, are shown as a function of radial distance from the axis. (c) The field heterogeneity, which is calculated using Eq. (2), is shown in (i) the x–z plane and (ii) the x–y plane. The axes have been normalized to the inner diameter of the magnet, $2R_i$, and the heterogeneity is expressed as a percentage. Each contour line represents a 10% change in field heterogeneity, with dark blue and dark red representing the smallest and largest percentage change, respectively.

extent of the field heterogeneity, provided that the outer diameter of the magnet is at least twice that of the inner diameter. In our case, we require a magnet with a minimum inner diameter of 40 mm since our region-of-interest cylinder has a diameter of 20 mm.

Figure 2 illustrates a ring magnet geometry that meets the criteria outlined in Sec. II. The magnets are commercial off-the-shelf neodymium–iron–boron (NdFeB) (N42) ring magnets of thickness 5 mm. We use three sizes: outer diameter (OD) 90 mm, inner diameter (ID) 64 mm; OD60, ID40; and OD40, ID25. The arrangement and positioning of the magnets are shown in Figs. 2(a) and 2(b), respectively. In total, there are 18 commercial magnets in the system, but these could be replaced with four custom-made magnets that have the same physical footprint and magnetic field strength. The design is composed of two halves that have exact-reflective symmetry about the $z = 0$ mm mirror line: one half contains the magnets positioned at z_1 and z_2 (colored purple and red, respectively), while the other half contains the magnets positioned at z_3 and z_4 (also colored red and purple, respectively). The red magnet groups comprise three magnet layers, with each layer consisting of two concentric ring magnets (OD90, ID64 and OD60, ID40) with the same polarity [see Fig. 2(a)]. The polarity between each adjacent face of the layers has the opposite magnetic field direction, and hence, the layers attract, resulting in zero separation between the layers. In reference to the two take home messages, the inner diameter of the red magnet group (ID40) is twice that of the diameter of the cylinder region of interest and the outer diameter of the red magnet group (OD90) is more than twice that of the inner diameter of the red magnet group.

The purple magnet groups comprise one magnet layer composed of three concentric ring magnets (OD90, ID64; OD60, ID40; and OD40, ID25) with the same polarity. Unlike the red magnet group, neither the inner diameter of the magnet is twice that of the diameter of the cylindrical region of interest, nor is the outer

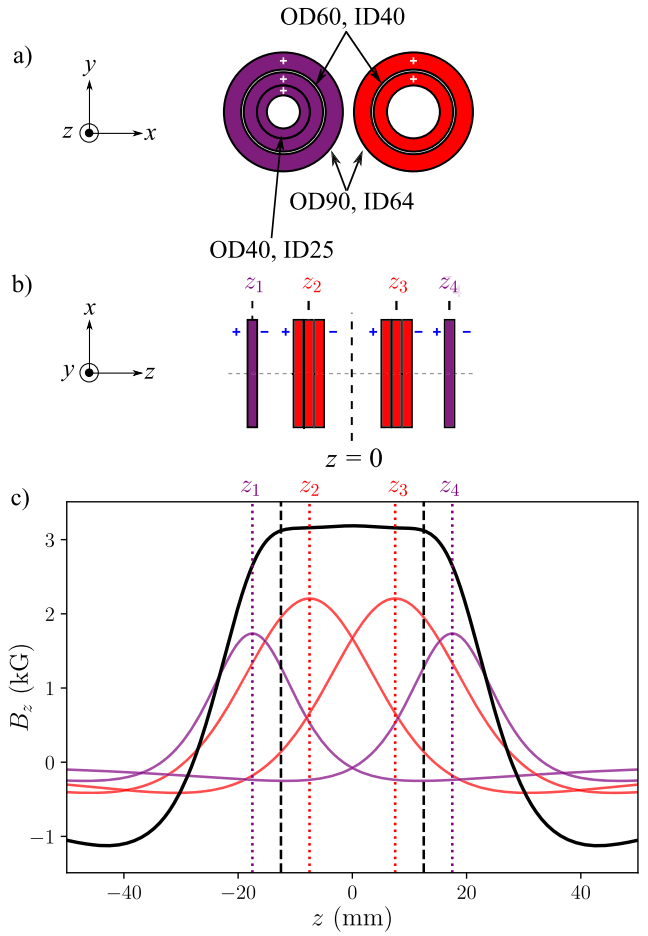

FIG. 2. (a) Illustration of the concentric magnet arrangement in the *x*–*y* plane used in the computation model. "OD" and "ID" correspond to the outer and inner diameters of the magnets, respectively, with the number succeeding either OD or ID indicating the dimension in millimeters. The design can be thought of as four magnet groups, illustrated by the use of two colors (purple and red) since the design is symmetric about the $z = 0$ mirror line. The red magnet groups consist of three magnet layers, with each layer containing two concentric magnets. The purple magnet groups consist of one magnet layer with three concentric magnets. The polarity of the magnets is shown by a white "plus" sign. (b) Illustration of the magnet arrangement in the *x*–*z* plane. The magnet groups are positioned accordingly: purple positioned at z_1, red at z_2, red at z_3, and purple at z_4. The polarity of magnet groups is shown by a blue "plus" and "minus" sign. (c) Theoretical calculation of the maximum axial magnetic field, B_z, using Eqs. (3) and (4) when the separation between each adjacent magnet group is zero. The field from each individual magnet group is shown and illustrated via their corresponding color, with the magnet group position shown using dotted lines and z_i label, where $i = 1$, 2, 3, or 4. The total magnetic field is a superposition of the fields from the four magnet groups and is shown via a black solid line. Also shown are vertical black dashed lines that define boundaries of the region of interest for the field homogeneity, where for this case, $B_{\text{mean}} = (3.16 \pm 0.02)$ kG with a root-mean-square field variation of less than 1%.

diameter of the magnet twice that of the inner diameter. To help understand the reason behind this and to be able to extract the positions of the magnet groups from our experimentally measured data, we need to know how to calculate the magnetic field for a ring magnet with defined physical dimensions at a particular position z. From this, the contribution of the magnetic field from the individual magnet groups to the total magnetic field can be calculated. Assuming a cylindrical magnet with uniform axial magnetization and $B_x = B_y = 0$, the longitudinal component of the magnetic field B_z[30] is given by

$$B_z(z) = \frac{B_0}{2}\left(\frac{z - z_0 + d}{\sqrt{(z - z_0 + d)^2 + R^2}} - \frac{z - z_0 - d}{\sqrt{(z - z_0 - d)^2 + R^2}}\right). \quad (3)$$

Here, $2d$ is the length of the cylinder, R is its radius, B_0 is the remanence field, and z_0 is the position of the cylinder's center along the z axis. The magnetic field for a ring is calculated using the principle of superposition. For a ring magnet with outer radius R_o and inner radius R_i, the field is that from a cylinder of radius R_o minus the field from a cylinder with R_i, i.e.,

$$B_z^{\text{ring}}(z) = B_z^{R_o}(z) - B_z^{R_i}(z). \quad (4)$$

The axial magnetic field for the arrangement in Figs. 2(a) and 2(b) can be calculated using Eqs. (3) and (4). The total field and the individual contributions from the four magnet groups are shown in Fig. 2(c). The vertical black dashed lines define the upper and lower boundary of the region-of-interest cylinder. The maximum mean axial magnetic field (i.e., when the separation between adjacent magnet groups is zero) between the two cell faces is $B_{\text{mean}} = (3.16 \pm 0.02)$ kG with a root-mean-square field variation of less than 1%. By changing the positions (z_1, z_2, z_3, and z_4) with respect to $z = 0$, we can change the magnetic field strength while still maintaining field homogeneity.

Figure 3 illustrates the maximum magnetic field profile in the *x*–*z* plane determined using MagPyLib for the magnet arrangement shown in Fig. 2. The computational code, which is available in the supplementary material, takes into account the hardware material thickness and incorporates this into the magnet group positions (z_1, z_2, z_3, and z_4). Since Fig. 3 shows the maximum field, the separation of the four magnet groups are defined by the thickness of the hardware material separating the magnets only. As shown in Fig. 3(a), the magnetic field strength is at its strongest inside the magnets, as expected, with a field inside the bore of ~2 to 3 kG. More interestingly, the field heterogeneity over the cylindrical volume of interest, as shown in Figs. 3(b) and 3(c), is within 12% and 4%, respectively. Although the length of the magnet assembly is less than the desired 50 mm (twice the length of the vapor cell, as stated in the first take home message), by including the additional magnet in the purple group, the field heterogeneity increases by a few percentage beyond the required 10% at the very edges. This is a small sacrifice to make at the expense of a more compact and lightweight instrument.

B. Hardware criteria

The magnet holder consists of two halves, which are mirror images of one another, and can be separated to permit insertion of a vapor cell to lie within the bore of the magnets. Each half consists of a square block and two cylinders, as shown in Fig. 4(a): one is defined as the "large" cylinder and the other is defined as the "small" cylinder. The large cylinders contain the red magnet group, and the small cylinders contain the purple magnet group, as shown in Fig. 2.

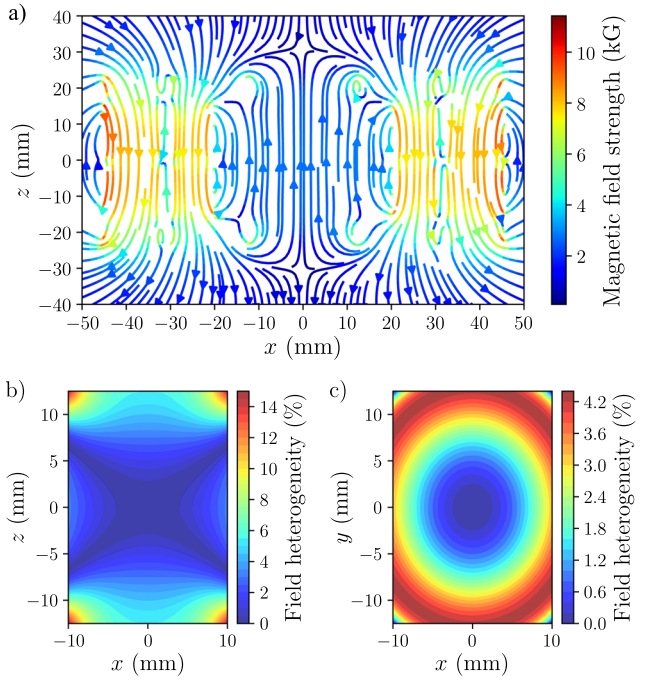

FIG. 3. MagPyLib magnetic field computation for the magnet assembly shown in Fig. 2 when taking into account the hardware constraints. The assembly has been set to produce the maximum magnetic field. (a) Magnetic field displayed in the *x*–*z* plane illustrated in magnitude by color and direction by arrows. Field heterogeneity calculated using Eq. (2) in the (b) *x*–*z* plane and (c) *x*–*y* plane. Each contour line represents a percentage change of 0.5% and 0.2% in (b) and (c), respectively.

The large cylinder back plate is threaded on the outside with a pitch of 2 mm and screws into the square block, permitting an axial translation of 2 mm per rotation. The thickness of the square block sets how much the large cylinder can translate longitudinally—a square block thickness of 20 mm is sufficient to produce the fields investigated in this paper. The front plate of the large cylinder is threaded on the inside of its bore with a pitch of 2 mm. The back plate of the small cylinder is threaded on the outside, which enables the small cylinder to be screwed into the internal bore of the large cylinder front plate. This permits an axial translation of the small cylinder of 2 mm per one full 2π rotation, with respect to the large cylinder. This pitch is sufficient to provide the tuning control we require. Photographs of the complete assembly are shown in Fig. 4(b). In the bottom photograph, the large imaging window is clearly visible. Figure 4(c) illustrates the maximum axial magnetic field strength measured for the magnets and hardware used in this design.[31] The mean axial magnetic field over the region of interest of $z = \pm 12.5$ mm is $B_{\text{mean}} = 2.67$ kG with a root-mean-square field variation of 90 G, which is less than 4% variation. Below, normalized residuals are also displayed. A Marquardt–Levenberg fit to experimental data and an amalgamation of Eqs. (3) and (4) result in the positions (z_1, z_2, z_3, and z_4) shown in the inset with their associated errors. The magnetic field profile within the region of interest exhibits more variation than that in Fig. 2(c). We attribute this to the material of the large cylinder back plate warping, leading to the OD60, ID40 magnets in the red group coming closer together than

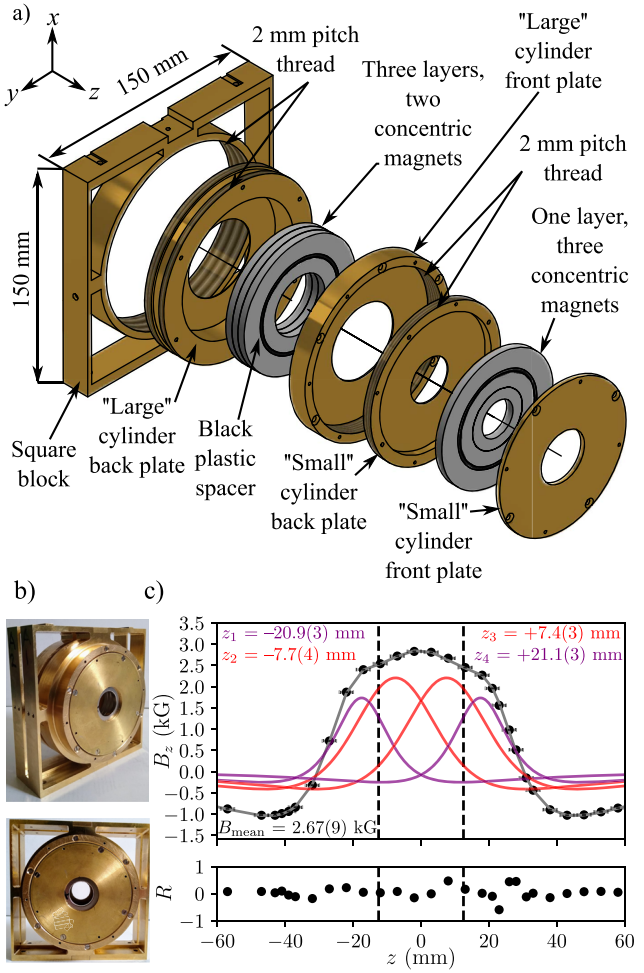

FIG. 4. (a) An exploded view schematic illustration of one half of the magnet holder, which is composed of a square block, a "large" cylinder, and a "small" cylinder. Also shown are the magnets and black plastic spacers. (b) Photographs of the complete assembly. (c) Measured magnetic field profile B_z (black dots) when the assembly is set to give a maximum field. The average magnetic field over the region of interest, illustrated via the dashed black lines, is $B_{\text{mean}} = 2.67$ kG with a root-mean-square deviation of 0.09 kG over this region, i.e., ≈4% rms variation. Also shown are the individual contributions from the four magnet groups that are colored accordingly, as outlined in Fig. 2, with the positions and corresponding errors extracted from the Marquardt–Levenberg fit (gray solid line)[32] using Eq. (3) and the experimental data. The normalized residuals, *R*, are also shown.

intended. This is evident from the magnet positions stated in the inset as they are smaller than the minimum separation predicted from the hardware material thickness. The warping material is only problematic at large magnetic fields (as evidenced by the lack of field variation in Fig. 5) and will be alleviated in future designs. The material chosen for the magnet holder is brass. Brass is non-magnetic and is durable enough to withstand cross-threading while screwing the cylinders closer together or further apart when tuning the magnetic field strength. To vary the cylinder positions, additional holes were included on each of the cylinder front plates such that custom tools could be inserted and used to rotate the cylinders and, hence,

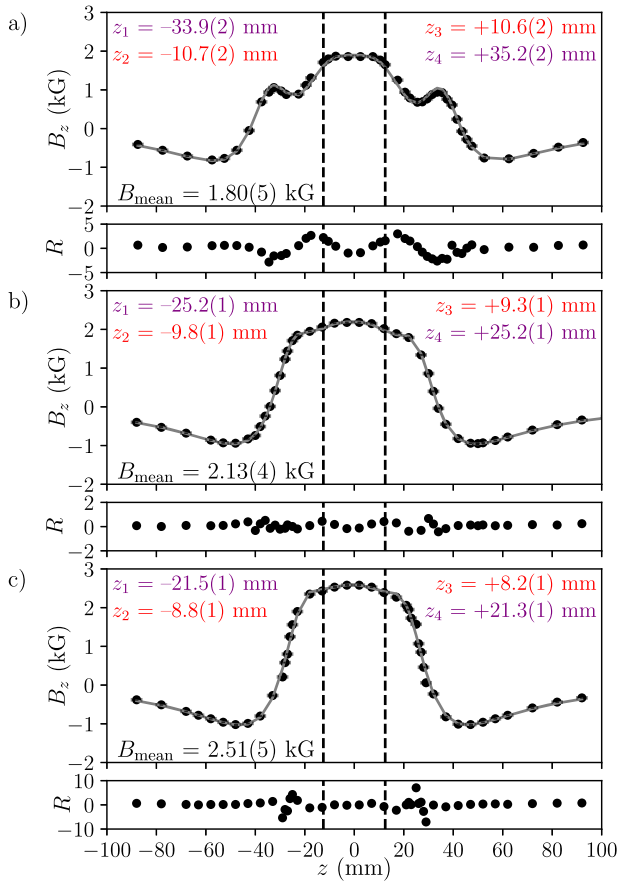

FIG. 5. Measured axial magnetic field (black dots) with an optimized fit (gray solid line) is shown for three arrangements of the magnet groups. The normalized residuals for each subplot are shown, as are the magnetic group positions, which have been extracted from the optimized fit. Vertical black dashed lines indicate the vapor cell face positions. The mean magnetic field along the length of the vapor cell, i.e., between the two vertical black dashed lines, and the root-mean-square deviation in (a) is B_{mean} = 1.80(5) kG, (b) is B_{mean} = 2.13(4) kG, and (c) is B_{mean} = 2.51(5) kG.

translate them. CAD drawings for these tools are included in the supplementary material.

III. RESULTS

In the remainder of this paper, we demonstrate how we can manipulate the magnetic field profile by varying the positions of the magnet groups using the hardware discussed in Sec. II B. We compare our measurements to theoretical calculations using Eqs. (3) and (4).

An axial Hall probe (AP002 probe used with Hirst Magnetic Instruments GM07 gaussmeter) was used to measure B_z longitudinally. Figure 5 shows three examples of the measured field profile. In each example, the maximum measured magnetic field is distinct due to different positioning of the magnet groups, as discussed in Sec. II A. The experimental data are fitted using Eqs. (3) and (4), where we have assumed that the magnet dimensions are fixed. We have extracted the positions of the four magnet groups and the remanence field using a Marquardt–Levenberg fit: the errors in the fit parameters are estimated using the square root of the diagonal elements of the covariance matrix.[32] The positions of the magnet groups, the mean magnetic field, and root-mean-square deviation within the region of interest, shown via a vertical dashed line, are stated in each subplot. Also shown are the associated normalized residuals for each subplot, which demonstrate excellent agreement between theory and experiment.

We learn a lot by extracting the magnet group positions and their associated errors: they tell us whether there is a fault with the hardware design, as demonstrated in Fig. 4(c) and discussed in Sec. II B; we can insert them into our MagPyLib code to extract the field heterogeneity using Eq. (2) to save us from measuring the entire field profile, and most importantly, we can use them to optimize the magnetic field heterogeneity. We see that in Fig. 5(a), we produce an axial magnetic field of 1.80(5) kG and we achieve homogeneity over a length of 25 mm as required. However, we see that we have two local field maxima at ~±40 mm. We attribute these to inappropriate small cylinder positions, and bringing the positions of the small cylinders closer to $z = 0$ will eradicate these. In spite of this, we have achieved the field required over the region of interest. As shown in Fig. 4(c), the maximum field we can achieve is B_{mean} = 2.67(9) kG due to the hardware constraints, as illustrated in Fig. 4(a). We can achieve any value of the field between the maximum and 1.80(5) kG; examples are shown in Figs. 5(b) and 5(c).

The radial component of the field B_x was measured using a transverse Hall probe (TP002 probe) when the instrument is set to give a maximum magnetic field of 2.67(9) kG. Figure 6 shows three examples of the measured radial field at different longitudinal positions [z = 0(1), +8(1), and −8(1) mm]. The uncertainties in the longitudinal positions have been estimated to include systematic errors on the zero position (i.e., $z = 0$ mm) and the tilt of the Hall probe. The black, red, and purple dotted lines represent the theoretical radial field extracted from the MagPyLib magnetic field code (which can be found in the supplementary material) at longitudinal positions z = 0 mm, z = +8 mm, and z = −8 mm, respectively. The data show excellent qualitative agreement between theory and verify our

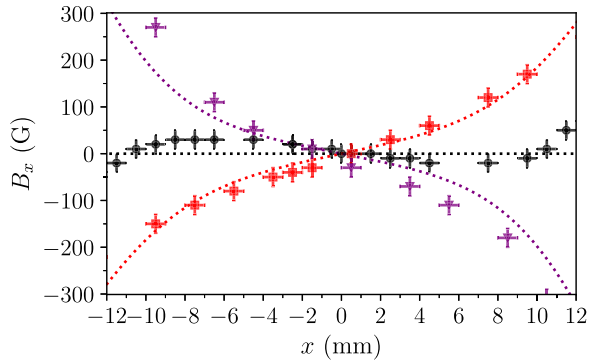

FIG. 6. Measured radial component B_x of the instrument measured at longitudinal positions z = 0(1) mm (black circles), z = +8(1) mm (red squares), and z = −8(1) mm (purple triangles). The instrument is set to give a mean axial magnetic field of B_{mean}, as illustrated in Fig. 4(c). The black, red, and purple dotted lines represent the theoretical radial field extracted from the MagPyLib magnetic field code at longitudinal positions z = 0 mm, z = +8 mm, and z = −8 mm, respectively.

original assumption that the radial component will have minimal contribution to the total magnetic field [as shown in Fig. 1(b)(ii)]. In fact, using Eq. (1), we see that the radial component contributes to 2% of the total magnetic field at these longitudinal positions within the instrument.

IV. CONCLUSION

In conclusion, we have presented a permanent magnetic field design that can produce an axial magnetic field of several kilogauss with field homogeneity over a length-scale of tens of millimeters, with less than 2% contribution from the radial field component. The hardware permits field tunability ranging from 1.80(5) to 2.67(9) kG with an rms field variation of less than 4%, and we demonstrate that Marquardt–Levenberg fits to experimental data demonstrate excellent agreement with theory. The design is such that a cylindrical vapor cell of length 25 mm and diameter 25 mm can be placed within the bore of the ring magnets, with a clear aperture of 20 mm for imaging through the vapor cell. The design will be of significance and benefit to those interested in atomic spectroscopy in large axial magnetic fields.

SUPPLEMENTARY MATERIAL

The supplementary material contains the MagPyLib python code for calculating the magnetic field profile of instrument, hardware CAD drawings (including drawings for jigs required for assembly and tuning tools), parts list (including a bill of materials) for the design discussed here, and assembly advice.

ACKNOWLEDGMENTS

I thank Ifan Hughes and Steven Wrathmall for helpful discussions, Clare Higgins and Thomas Cutler for editorial discussions, Stephen Lishman and Malcolm Robertshaw for mechanical design assistance and fabrication, and the anonymous referees for constructive feedback. I also acknowledge EPSRC (Grant No. EP/R002061/1) and STFC (Grant No. ST/V005979/1) for funding.

AUTHOR DECLARATIONS

Conflict of Interest

The author has no conflicts of interest to disclose.

DATA AVAILABILITY

The data that support the findings of this study are openly available in DRO at https://doi.org/10.15128/r2xs55mc08w.[33]

REFERENCES

[1] S. A. Hopkins, K. Butler, A. Guttridge, S. Kemp, R. Freytag, E. A. Hinds, M. R. Tarbutt, and S. L. Cornish, Rev. Sci. Instrum. **87**, 043109 (2016).
[2] P. Cheiney, O. Carraz, D. Bartoszek-Bober, S. Faure, F. Vermersch, C. M. Fabre, G. L. Gattobigio, T. Lahaye, D. Guéry-Odelin, and R. Mathevet, Rev. Sci. Instrum. **82**, 063115 (2011).
[3] M. A. Zentile, D. J. Whiting, J. Keaveney, C. S. Adams, and I. G. Hughes, Opt. Lett. **40**, 2000 (2015).
[4] X. Shan, X. Sun, J. Luo, Z. Tan, and M. Zhan, Appl. Phys. Lett. **89**, 191121 (2006).
[5] L. Weller, K. S. Kleinbach, M. A. Zentile, S. Knappe, I. G. Hughes, and C. S. Adams, Opt. Lett. **37**, 3405 (2012).
[6] Y. Yong, C. Xuewu, L. Faquan, H. Xiong, L. Xin, and G. Shunsheng, Opt. Lett. **36**, 1302 (2011).
[7] Y. Xia, X. Cheng, F. Li, Y. Yang, X. Lin, J. Jiao, L. Du, J. Wang, and G. Yang, Appl. Opt. **59**, 1529 (2020).
[8] P. Chang, Y. Chen, H. Shang, X. Guan, H. Guo, J. Chen, and B. Luo, Appl. Phys. B: Lasers Opt. **125**, 230 (2019).
[9] X. Miao, L. Yin, W. Zhuang, B. Luo, A. Dang, J. Chen, and H. Guo, Rev. Sci. Instrum. **82**, 086106 (2011).
[10] F. S. Ponciano-Ojeda, F. D. Logue, and I. G. Hughes, J. Phys. B: At., Mol. Opt. Phys. **54**, 015401 (2021).
[11] D. J. Whiting, R. S. Mathew, J. Keaveney, C. S. Adams, and I. G. Hughes, J. Mod. Opt. **65**, 713 (2018).
[12] B. A. Olsen, B. Patton, Y.-Y. Jau, and W. Happer, Phys. Rev. A **84**, 063410 (2011).
[13] A. Sargsyan, G. Hakhumyan, C. Leroy, Y. Pashayan-Leroy, A. Papoyan, D. Sarkisyan, and M. Auzinsh, J. Opt. Soc. Am. A **31**, 1046 (2014).
[14] A. Cacciani, D. Ricci, P. Rosati, E. J. Rhodes, E. Smith, S. Tomczyk, and R. K. Ulrich, Nuovo Cimento C **13**, 125 (1990).
[15] M. B. Korsós, P. Chatterjee, and R. Erdélyi, Astrophys. J. **857**, 103 (2018).
[16] M. B. Korsós, M. K. Georgoulis, N. Gyenge, S. K. Bisoi, S. Yu, S. Poedts, C. J. Nelson, J. Liu, Y. Yan, and R. Erdélyi, Astrophys. J. **896**, 119 (2020).
[17] R. Erdelyi, M. B. Korsos, X. Huang, Y. Yang, D. Pizzey, S. A. Wrathmall, I. G. Hughes, M. Dyer, V. S. Dhillon, B. Belucz, R. Brajsa, P. Chatterjee, X. Cheng, Y. Deng, S. V. Dominguez, R. Joya, P. Gomory, N. G. Gyenge, A. Hanslmeier, A. Kucera, D. Kuridze, F. Li, Z. Liu, X. Long, M. Mathioudakis, S. Matthews, J. R. T. McAteer, A. A. Pevtsov, W. Potzi, P. Romano, J. Shen, J. Temesvary, A. G. Tlatov, C. Triana, D. Utz, A. M. Veronig, Y. Wang, Y. Yan, T. Zaqarashvili, and F. Zuccarello, "The Solar Activity Monitor Network-SAMNet," J. Space Weather Space Clim. (published online, 2021).
[18] M. Cimino, A. Cacciani, and N. Sopranzi, Sol. Phys. **3**, 618 (1968).
[19] G. Agnelli, A. Cacciani, and M. Fofi, Sol. Phys. **44**, 509 (1975).
[20] M. A. Zentile, J. Keaveney, L. Weller, D. J. Whiting, C. S. Adams, and I. G. Hughes, Comput. Phys. Commun. **189**, 162 (2015).
[21] R. Speziali, A. Di Paola, M. Centrone, M. Oliviero, D. Bonaccini Calia, L. Dal Sasso, M. Faccini, V. Mauriello, and L. Terranegra, J. Space Weather Space Clim. **11**, 22 (2021).
[22] W. Kiefer, R. Löw, J. Wrachtrup, and I. Gerhardt, Sci. Rep. **4**, 6552 (2014).
[23] D. J. McCarron, I. G. Hughes, P. Tierney, and S. L. Cornish, Rev. Sci. Instrum. **78**, 093106 (2007).
[24] I. Gerhardt, Opt. Lett. **43**, 5295 (2018).
[25] B.-M. Ma and K. S. V. L. Narasimhan, J. Magn. Magn. Mater. **54–57**, 559 (1986).
[26] M. Ortner and L. G. Coliado Bandeira, SoftwareX **11**, 100466 (2020).
[27] M. Haavisto, S. Tuominen, T. Santa-Nokki, H. Kankaanpää, M. Paju, and P. Ruuskanen, Adv. Mater. Sci. Eng. **2014**, 760584.
[28] R. S. Caprari, Meas. Sci. Technol. **6**, 593 (1995).
[29] F. J. Salazar, F. J. Nieves, A. Bayón, and F. Gascón, Rev. Sci. Instrum. **88**, 095107 (2017).
[30] L. Weller, *Absolute Absorption and Dispersion in a Thermal Rb Vapour at High Densities and High Magnetic Fields* (Durham University, 2013).
[31] Note that the thickness of the front and back plates should be taken into account when simulating the magnetic field in MagPyLib (see the supplementary material for a further discussion).
[32] I. G. Hughes and T. P. A. Hase, *Measurements and Their Uncertainties: A Practical Guide to Modern Error Analysis* (OUP, Oxford, 2010).
[33] The data presented in this paper are available from DRO https://doi.org/10.15128/r2xs55mc08w.